Inorganic Chemistry
Article
pubs.acs.org/IC

# Defects in Chemically Synthesized and Thermally Processed ZnO Nanorods: Implications for Active Layer Properties in Dye-Sensitized Solar Cells

Partha Pratim Das,[†,∥] Shruti A. Agarkar,[§,∥] Soumita Mukhopadhyay,[†,∥] Unnikrishnan Manju,[‡] Satishchandra B. Ogale,[§,∥] and P. Sujatha Devi*[,†,∥]

[†]Nano-Structured Materials Division, and [‡]Materials Characterization Division, CSIR-Central Glass and Ceramic Research Institute, Kolkata 700 032, India

[§]Physical and Materials Chemistry Division, CSIR-National Chemical Laboratory, Pune 411 008, India

[∥]CSIR-Network Institute of Solar Energy (CSIR-NISE), New Delhi 110 012, India

*Supporting Information*

**ABSTRACT:** We have carried out the effect of post annealing temperatures on the performance of solution-grown ZnO rods as photoanodes in dye-sensitized solar cells. Keeping our basic objective of exploring the effect of native defects on the performance of DSSC, we have synthesized ZnO rods having length in the range of 2−5 $\mu$m by a modified sonication-induced precipitation technique. We performed extensive characterization on the samples annealed at various temperatures and confirmed that annealing at 300 °C results in ZnO rods with minimum native defects that have been identified as doubly ionized oxygen vacancies. The electron paramagnetic resonance measurements on the samples, on the other hand, confirmed the presence of shallow donors in the low temperature annealed samples. We also carried out electrochemical impedance measurements to understand the transport properties at different interfaces in the solar cell assembly. We could conclude that solution-processed ZnO rods annealed at 300 °C are better suited for fabricating DSSC with improved efficiency (1.57%), current density (5.11 mA/cm$^2$), and fill factor (45.29%). On the basis of our results, we were able to establish a close connection between the defects in the metal oxide electron transporting nano system and the DSSC performance.

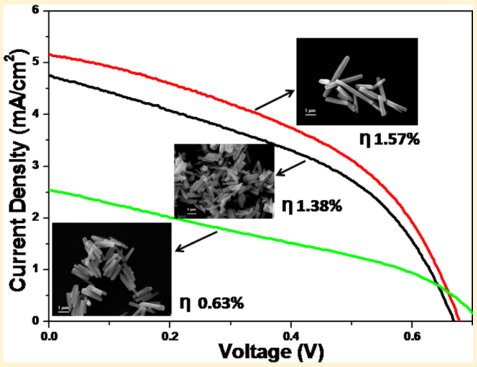

## ■ INTRODUCTION

The next generation of photovoltaic devices, dye-sensitized solar cells (DSSCs), have recently received more attention because of their added advantages as compared to conventional photovoltaic devices.[1−4] As a result, considerable emphasis has been given to $TiO_2$-based DSSC resulting in overall conversion efficiencies of 11−15%.[1−5] ZnO, as a compatible photoanode material, is also being explored as an alternative material to $TiO_2$ due its large band gap (3.44 eV), high electron mobility (205−1000 cm$^2$ V$^{-1}$ S$^{-1}$), high exciton binding energy (60 meV), high electron affinity (4.5 eV), and effectiveness in tailoring the morphology and properties.[5] ZnO in various morphologies, nanocrystals/nanoparticles, nanowires, nanospheres, nanotubes, flowers, rods, etc., have been used in the fabrication of DSSC.[5−9] However, the power conversion efficiencies obtained in ZnO-based DSSCs are normally lower as compared to $TiO_2$-based ones.[5−9] In certain cases, efficiencies as high as 7% have been reported for ZnO-based DSSCs, but these values are still lower as compared to $TiO_2$-based DSSCs.[1−9] The value of reported efficiencies for various ZnO structures is very wide and ranges from as low as 0.02% to as high as 7%.[6−11] Nevertheless, because ZnO has an order of magnitude higher electron mobility as compared to $TiO_2$, there is still ample scope and opportunity to improve the efficiency of ZnO-based DSSC. The lower efficiency of ZnO as compared to $TiO_2$ has been thought to be mainly due to the dissolution of ZnO leading to the formation of dye−$Zn^{2+}$ aggregates especially under acidic conditions, and the slow electron-injection flow from dye.[6,12−14] Therefore, most of the studies pertaining to higher efficiencies have been carried out with N719 dye molecules having a lower number of carboxyl groups than the N3 dye.[5−9] Among the various structures investigated thus far, one-dimensional structures such as ZnO rods and wires have exhibited better performance due to improvement in the directionality of transport of the injected electron by avoiding particle to particle hopping, increase in the electron diffusion length, and also the decreased recombination.[6,7,15,16] Therefore, the tendency to explore simple methodologies to grow one-dimensional (1D) ZnO nanostructures has induced great interest in this area of research and development. Various methods have been reported to date, to synthesize ZnO rods such as metallorganic chemical vapor deposition, template-based methods, laser ablation, spray pyrolysis technique, and

**Received:** May 13, 2013
**Published:** March 31, 2014

various other chemical processing techniques.[6−9] However, studies focused on the influence of native defects present in ZnO rods on the performance of fabricated DSSCs are scarce, albeit a large number of publications are available on the synthesis, properties, applications, and device performance of ZnO (refs 6−9 and references therein). Among the few reports available on the defect related DSSC performance, the paper by Hsu et al., on the performance of ZnO rods prepared by hydrothermal and vapor deposition techniques, is noteworthy.[17] Wong et al., on the other hand, investigated the influence of optical properties of ZnO particles on the DSSC performance, whereas Lou et al. reported the influence of defect density on ZnO rods and Makhal et al. reported the role of resonance energy light based on defect emission in ZnO.[18−20] Therefore, our basic objective was to investigate and correlate the influence of native defects on the solution processed ZnO rods and their thermally annealed counterparts and their performance as photo anodes in DSSC. Here, we have prepared ZnO rods by a sonication-induced precipitation methodology followed by simple heating in an aqueous media at 80 ± 5 °C for 6 h. We have investigated in detail the properties of the prepared ZnO rods and have revealed an interesting correlation between the structural defects, photoluminescence properties, and solar cell performances of DSSC fabricated using the as-prepared and thermally annealed ZnO rods.

## EXPERIMENTAL SECTION

**Materials and Synthesis of ZnO Rods.** The samples have been prepared by sonochemical method using $NH_4OH$ and zinc acetate as the starting materials. In a typical reaction, ammonia solution [30% GR, Merck Ltd. Mumbai, India] was added dropwise to 250 mL of 0.1 M zinc acetate [$(CH_3COO)_2Zn\cdot 2H_2O$, Merck, Germany] solution, under sonication (ultrasonic power 250 W, ultrasonic frequency 25 kHz, probe diameter 25 mm) until the pH reached 9. The pH was fixed slightly above 9, the isoelectric point (IEP) of ZnO. A slow addition of ammonia was critical in getting a homogeneous precipitate, and hence the required amount of ammonia was added dropwise for an hour until complete precipitation of the hydroxide has occurred. The precipitate was centrifuged and further dispersed in 400 mL of water and stirred on a magnetic stirrer for 6 h, maintaining the solution temperature at 80 ± 5 °C. The precipitate was then centrifuged at an average rpm of 10 000 for 10 min followed by washing with distilled water and drying under IR lamp around 70 °C. The as-synthesized powder was calcined at 100, 200, 300, 400, 500, and 600 °C, respectively, for 4 h for further studies. The 300 °C annealed sample has been further annealed in flowing oxygen and hydrogen atmospheres under identical conditions.

**Material Characterization.** The dried powder was characterized for structural properties by powder X-ray diffraction (XRD) analysis on a X'pert pro MPD XRD of PAN analytical with Cu $K_\alpha$ radiation ($\lambda$ = 1.5406 Å). The morphology of the synthesized powder was monitored on a scanning electron microscope (SEM), (LEO 430i, Carl Zeiss). The morphology of the rods was further monitored using transmission electron microscopy (TEM), which was carried out on a Tecnai G2 30ST (FEI) high-resolution transmission electron microscope operating at 300 kV. Fourier transform-infrared (FT-IR) spectra have been measured between 4000 and 400 $cm^{-1}$ with 200 scans on a NICOLET 5700 FTIR spectrometer with a resolution of 4 $cm^{-1}$. Potassium bromide (FTIR grade ≥99% trace metal basis) was used to prepare pellets (Sigma Aldrich (Germany), Pdt. Code: 101108329). The as-received KBr was oven-dried overnight at ~100 °C and then stored in a desiccator prior to use. The ratio of sample:KBr was varied as 1:2, 1:4, 1: 8, 1:16 to optimize the back ground signal, and the mixture was ground properly to prepare the pellets having thickness of around 0.15 mm. The specific surface area of the calcined samples was measured by Brunauer−Emmett−Teller (BET) method on a Quantachrome Instrument (NOVA 4000 E series). The diffuse reflectance (DR) spectra before and after dye loading were measured on a UV−vis−NIR spectrometer (Shimadzu UV-3600) to find out the extent of dye loading on the ZnO rods. The optical properties of the rods were further evaluated by recording the room-temperature photoluminescence spectrum (PL) on a steady-state spectrofluorometer (QM-40, Photon Technology International, PTI) using a xenon lamp (150 W) as an excitation source, at an excitation wavelength of 345 nm and band-pass of 5 nm. The zeta potential measurements have been carried out on a Horiba Nanoparticle Analyzer SZ100. Raman spectra were obtained using a Renishaw InVia Reflex micro Raman spectrometer with excitation of argon ion (514 nm) lasers. The spectra were collected with a resolution of 1 $cm^{-1}$. X-ray photoemission spectroscopy measurements were carried out in a PHI 5000 Versa probe II scanning XPS microprobe (ULVAC-PHI, U.S.). The measurements were performed at room temperature and at a base pressure better than $6 \times 10^{-10}$ mbar. All spectra were recorded with monochromatic Al $K_\alpha$ ($h\nu$ = 1486.6 eV) radiations with a total resolution of about 0.7 eV and a beam size of 100 $\mu$m. The X band EPR spectra for powder samples were measured on a Bruker EMX spectrometer at room temperature where the microwave frequency was measured with a Hewlett-Packard 5246 L electronic counter. Five milligrams of the sample was taken in a quartz tube of 1 mm diameter. Instrumental parameters of the spectrometer are frequency = 9.45 GHz, $B_O$-field = 346 mT, $B_O$-sweep = 200 mT, mod amplitude = 0.2 mT, and sweep time = 60 S.

**Fabrication of the Dye-Sensitized Solar Cell.** The ZnO films were made by the doctor blade method on FTO glass (7 $\Omega/cm^2$) and annealed at 450 °C for 1 h. The thickness of ZnO film was ~12 $\mu$m. For sensitization, these films were dipped in 0.5 mM N719 dye in ethanol for 4 h at room temperature. The sensitizer-coated ZnO films were washed with ethanol after removing from the dye. The electrolyte used was prepared using 0.6 M 1,2-dimethyl 3-propylimidazolium iodide, 0.1 M LiI, 0.05 M $I_2$, and 0.5 M 4-*tert*-butylpyridine in acetonitrile. Platinum nanoparticle-coated FTO was used as a counter electrode. The Pt paste has been purchased from Solaronix, Switzerland having Pt particles in the 10−20 nm size range. *I*−*V* characteristics were measured using a solar simulator (Newport) at 100 mW/$cm^2$ (1 sun AM 1.5). Standard silicon solar cell (SER NO. 189/PVM351) from Newport, U.S. was used as a reference cell. We have used a mask for measurement, and the active area of the cell was 0.25 $cm^2$. The details of the cell fabrication and paste making are reported elsewhere.[21] The data presented are an average of measurements taken on five different devices for each sample. Electrochemical impedance spectroscopy (EIS, Autolab PGSTAT30) was used to characterize the devices further. The frequency range chosen for the impedance measurement was from $10^{-2}$ to $10^6$ Hz with an AC amplitude of 10 mV, and the measurements were carried out at room temperature.[21]

## RESULTS AND DISCUSSION

**Structure and Microstructural Studies.** To confirm the phase formation, we have carried out room-temperature powder X-ray diffraction studies on three selected samples: the as-synthesized dried sample, the sample annealed at 300 °C, and the sample annealed at 600 °C, respectively (Supporting Information Figure S1). The XRD patterns matched well with the reported reference pattern of wurtzite ZnO (hexagonal phase, JCPDS card 36-1451), thus confirming the in situ formation of ZnO with high crystallinity during the synthesis. The calculated lattice parameters of the as-prepared samples were *a* = 3.251 Å and *c* = 5.212 Å, respectively, with a *c*/*a* ratio of 1.6031. We did not find much variation in the *c*/*a* ratio on calcination, an indication of the lattice stability. After being annealed at 300 °C, the sample exhibited a minor change in the lattice constants with *a* = 3.252 Å and *c* = 5.208 Å, respectively. The calculated unit cell volume for all three samples was higher than the volume calculated for the standard ZnO. The details

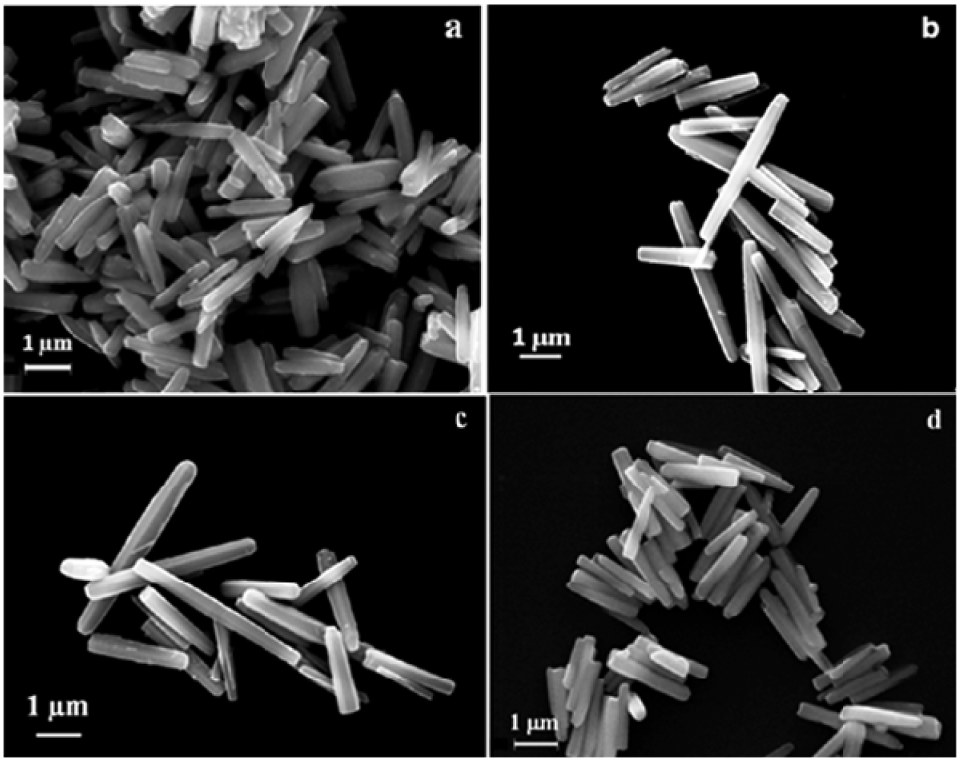

**Figure 1.** SEM images of (a) as-prepared ZnO rods, (b and c) rods annealed at 300 °C, and (d) rods annealed at 600 °C, respectively.

are given in Table S1 in the Supporting Information. The increase in unit cell volume could arise due to the presence of defects in the samples. The unit cell volume of the 300 °C annealed sample was the lowest, indicating lower defect concentration as compared to others.

To find out the morphology of the ZnO formed, we have carried out scanning electron microscopic studies on selected samples as shown in Figure 1a−d. It is evident from the SEM images that the process has resulted in the formation of ZnO rods in the as-prepared stage itself with an average length of 2 μm and diameter of ~350 nm (Figure 1a). The rods were agglomerated in the as-prepared stage, but on annealing at 300 °C, a minor increase in the rod length was noticed with a slight improvement in the nature of aggregation (Figure 1b and c), indicating the formation of separated rods. Interestingly, on further increase in the annealing temperature, the rods started to fuse and sinter as evident from the formation of grain boundaries in some of the rods shown for the 600 °C annealed sample (Figure 1d).

The TEM pictures of the 300 °C annealed rods dispersed in ethanol are presented in Figure 2a−c. A couple of rods that grew adjoining to each other are shown in Figure 2a. The diameter of the rods varied in the range 20−200 nm and length 4 μm or more. One end of the individual rod was tapered and pointed, while the other end was shaped like a hemisphere. The HRTEM image confirms the single crystalline nature of individual rods, where the spacing corresponds to (002) reflection. The SAED pattern shown in Figure 2c indicates the (110) and (100) planes of ZnO.

**Formation of ZnO Rods.** The pH of the solution during the precipitation of $Zn(OH)_2$ was maintained at 9 to arrest the formation of soluble $Zn(NH_3)_4^{2+}$ (eqs 1 and 2).[22] The centrifuged precipitate was again dispersed in water and was stirred on a magnetic stirrer at 80 ± 5 °C to induce the growth of ZnO crystallites.

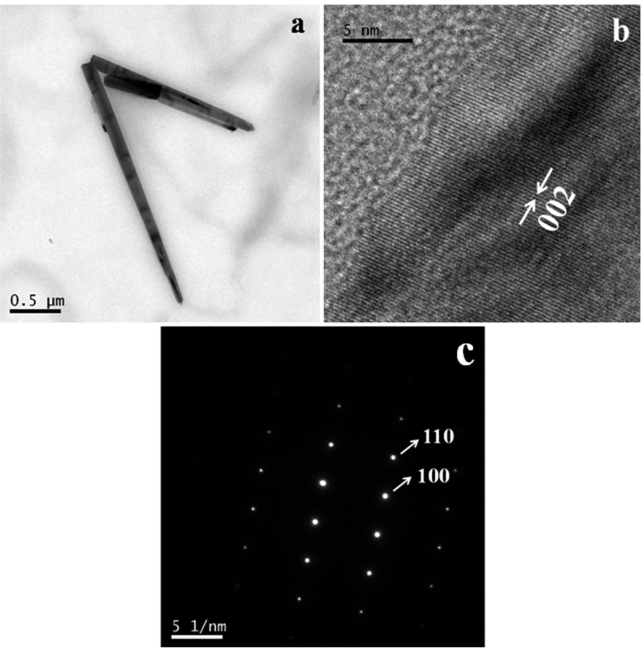

**Figure 2.** TEM images of ZnO rods annealed at 300 °C: (a) separated rods, (b) HRTEM image of a single rod, and (c) SAED pattern.

$$Zn(CH_3COO)_2\cdot 2H_2O + 2NH_4OH \rightarrow Zn(OH)_2 + 2NH_4(CH_3COO) \quad (1)$$

$$Zn(OH)_2 + 2H_2O \xrightarrow{\Delta} ZnO \quad (2)$$

In a typical Wurtzite structure of ZnO, the basal polar plane is (001), which terminates to positively charged $Zn^{2+}$, resulting in a large surface energy for the polar surfaces. Because no chelating agent was added during the synthesis, all of the planes are exposed for growth, resulting in a randomly oriented rod structure, unlike the growth in the presence of capping agents. The more rapid is the growth rate, the quicker will be the disappearance of the basal plane (0001), leading to the formation of rodlike ZnO with pointed or tapered shapes.[23]

**Optical Properties.** To evaluate the effect of annealing temperatures on the optical properties of the prepared ZnO powder, we have annealed the as-prepared ZnO at various temperatures from room temperature to 600 °C at an interval of 100 °C. The room-temperature absorption and photoluminescence (PL) studies have been carried out using the ethanol dispersion of prepared ZnO samples. The absorption spectrum is shown in Supporting Information Figure S2, and the emission spectrum is shown in Figure 3, respectively. All the samples exhibited a narrow absorption band at 380 nm, which is slightly red-shifted as compared to the reported bulk ZnO values. With an increase in the annealing temperature, the absorption peak shifts slightly toward higher wavelength, suggesting the presence of defects in these samples. The 600 °C annealed sample exhibited the maximum red shift as is clear from Supporting Information Figure S2g. In Figure 3a–g, the evolution of the photoluminescence bands with annealing temperature from 100 to 600 °C is presented. Usually, two emission bands were observed for ZnO: the near band edge emission (NBE) in the UV region, which originates from the recombination of free excitons, and the visible band emission (known as deep level emission, DLE), which arises due to the impurities or structural defects such as interstitial zinc and oxygen vacancies.[24−26] By carefully monitoring the optical properties, with annealing temperatures, it was observed that NBE is enhanced constantly with annealing temperatures from 100 to 300 °C with a concurrent increase/decrease in intensity of the defect related emission. Surprisingly, the intensity of NBE starts to decrease with further increase in annealing temperature and drops even below the as-prepared sample above 400 °C, followed by an increase in the intensity of the visible emission. In addition, the visible emission peak intensity has slowly shifted toward red with increase in the annealing temperature. As is evident from Figure 3a, the PL of the as-prepared ZnO exhibited a strong band near UV centered at 383 ± 2 nm (3.23 eV) and another broad visible band centered at 567 ± 2 nm (2.186 eV). With increase in the annealing temperature, up to 200 °C, the band position shifted slightly to the red, but with an increase in the intensity. At 300 °C, a sudden decrease in the visible PL band intensity was noticed with a consequent substantial increase in the near band edge emission at 385 nm. Clearly, the intensity of the 567 ± 2 nm (2.186 eV) band has decreased considerably after annealing at 300 °C, but slightly red-shifted to 596 ± 2 nm (2.080 eV). Surprisingly, above 300 °C, a noticeable increase in the visible band emission with a subsequent increase in the band intensity followed by a dramatic decrease in the intensity of the band edge emission was noticed. As is evident from Figure 3g, the 600 °C annealed sample exhibited a strong broad visible emission around 625 nm. Because the 300 °C annealed sample exhibited the lowest defect related emission, we have further annealed the 300 °C sample in flowing hydrogen and oxygen atmospheres for collecting more insight into the type of defects present in these samples. The normalized PL data of the sample are shown in the Supporting Information as Figure S3. There was not much change in the NBE emission, but a decrease in the intensity of the defect related emission was noticed as shown in the inset of Supporting Information Figure S3. The detailed discussion on the defect related emission properties will be presented in the defect structure of ZnO (vide infra).

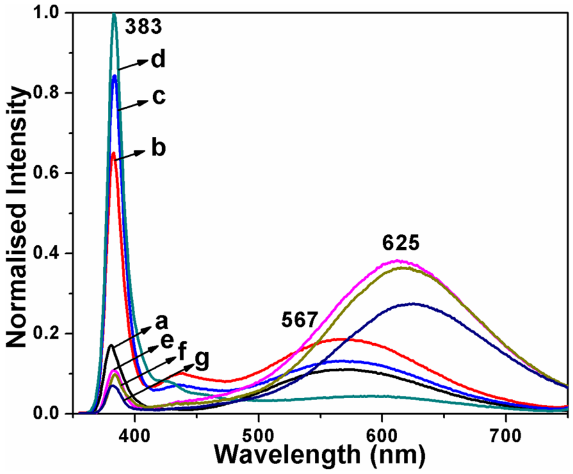

**Figure 3.** Normalized photoluminescence spectra of (a) as-prepared, (b) 100, (c) 200, (d) 300, (e) 400, (f) 500, and (g) 600 °C, respectively.

**Raman Spectral Studies.** To further assess the structural quality of the prepared samples, we have characterized the ZnO rods by Raman spectroscopy. The Raman spectrum of ZnO rods excited with the 514 nm $Ar^+$ laser line at room temperature is presented in Figure 4 for all of the calcined samples. The Raman spectrum is highly sensitive to crystalline nature, structural disorder, and defects in crystalline materials. Among the eight sets of optical modes for single-crystalline wurtzite ZnO, the $A_1$, E, and $E_2$ modes are Raman active. The A1 and E1 modes are polar and split into transverse-optical (TO) and longitudinal-optical (LO) phonons, and the E2 mode consists of two modes of low- and high-frequency phonons.[27] The most dominant and sharp peak at 438 $cm^{-1}$ observed in the Raman spectrum of all of the samples is the

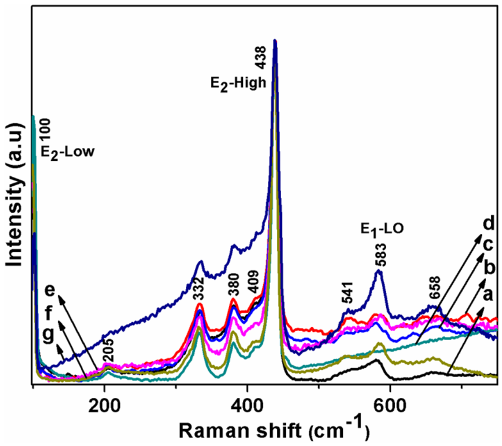

**Figure 4.** Raman spectra of the ZnO rods (a) as-prepared and annealed at (b) 100, (c) 200, (d) 300, (e) 400, (f) 500, and (g) 600 °C, respectively.

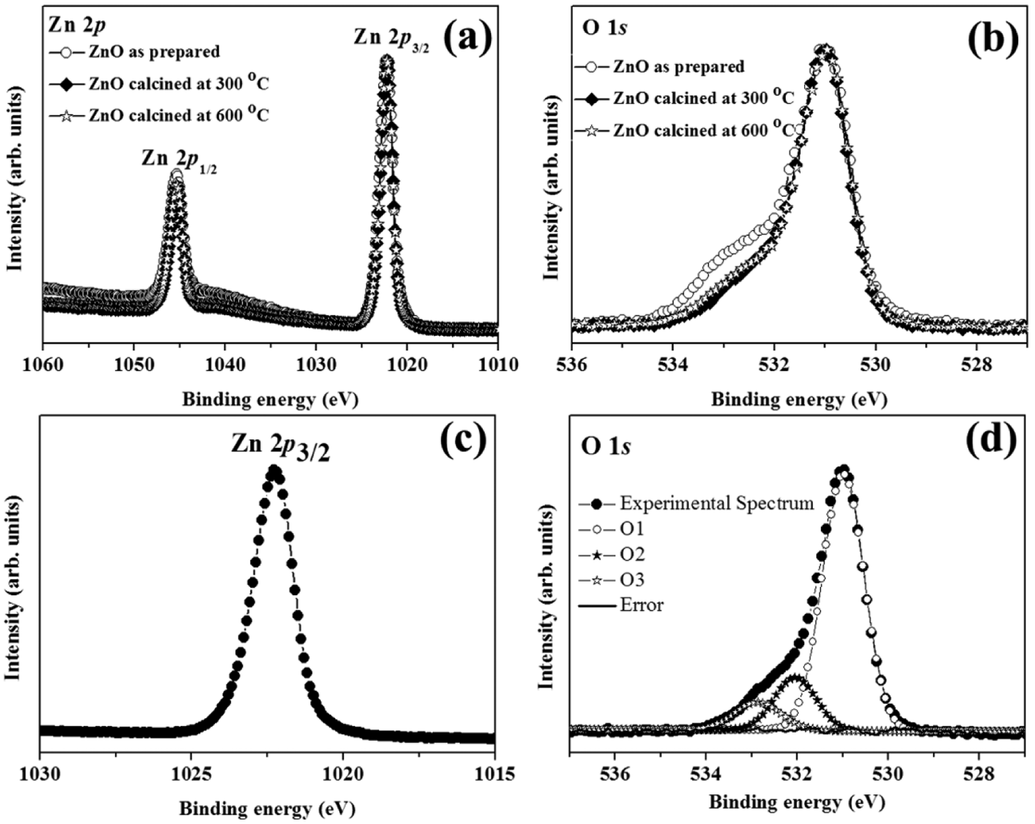

**Figure 5.** XPS spectra of (a) spin−orbit split peaks of Zn $2p_{3/2}$ of as-prepared and calcined samples, (b) O 1s spectra of as-prepared and calcined samples, (c) spin−orbit split peaks of Zn $2p_{3/2}$ showing a symmetric peak for the 300 °C annealed sample, and (d) spectral decomposition of O 1s spectra shows three different types of oxygen, represented as O1, O2, and O3 of the ZnO rods annealed at 300 °C.

intrinsic Raman-active $E_2$ mode characteristic of hexagonal wurtzite phase of ZnO.[27] The modes at 205, 332, and 658 $cm^{-1}$ are due to the multiphonon scattering processes (shown as dotted lines in the figure). On the other hand, the E1(LO) mode at 583 $cm^{-1}$, which appeared as a suppressed peak, is due to the presence of defects such as oxygen vacancies or oxygen interstitial.[27−29] Interestingly, the intensity of this peak was minimum for the as-prepared ZnO rods and was almost absent for the 300 °C annealed sample, confirming the formation of ZnO rods with minimum surface defects at this temperature.[27−29] It is interesting to note that the E1 (LO) phonon mode around 583 $cm^{-1}$ in the high-temperature-annealed sample has gone high in intensity as compared to 300 °C annealed sample. At 600 °C annealed sample, the 583 $cm^{-1}$ peak has become asymmetric with the appearance of another broad shoulder at 541 $cm^{-1}$. This could be due to the presence of interstitial oxygen in the high temperature annealed samples. The weaker band at 409 $cm^{-1}$ is assigned to the E1(TO) mode, and that at 380 $cm^{-1}$ is due to the A1(LO) mode, respectively.

**X-ray Photoemission Spectroscopy Studies.** For a further understanding of the electronic structure of these systems, selected members of the series, as-prepared, 300 °C annealed, and 600 °C annealed ZnO samples, were investigated by X-ray photoemission spectroscopy (XPS) technique. Zn 2p and O 1s core level spectra from the above-mentioned samples are shown in Figure 5a and b, respectively. The Zn 2p spectra for all of the samples are composed of the spin−orbit split peaks of Zn $2p_{1/2}$ and $2p_{3/2}$ appearing at around 1045.3 and 1022.2 eV binding energies, respectively. Apart from the slightly higher background for the as-prepared sample, Zn 2p spectra of all of the samples are approximately similar with respect to their spectral shapes and binding energy positions. However, the O 1s core level spectra show strong shoulders/asymmetries at the higher binding energy side, the highest for the as-prepared sample and strongly suppressed with annealing, with the 300 °C annealed ZnO rods having the lowest shoulder intensities. We performed a detailed core level analysis of the 300 °C annealed sample. An expanded view of the Zn $2p_{3/2}$ core level spectra obtained from the 300 °C annealed sample is shown in Figure 5c. The symmetric shape of the spectra together with its binding energy position at around 1022.2 eV could be assigned to Zn in $Zn^{2+}$ state in ZnO.[30] A spectral deconvolution of the asymmetric O 1s spectrum of the sample annealed at 300 °C, depicted in Figure 5d, results in three components appearing at binding energies of 530.95, 531.95, and 532.85 eV, respectively. On the basis of the reported results by many investigators, it can be concluded that the 530.95 eV ($O_1$) component on the lower binding energy side of the O 1s spectrum belongs to $O^{2-}$ ions in Zn−O bonds of wurtzite structure (lattice oxygen). The medium binding energy peak at 531.95 eV (O2) is associated with the $O^{2-}$ ions in oxygen-deficient regions within the ZnO matrix. Finally, the high binding energy portion at 532.85 eV (O3) is generally attributed to the presence of interstitial oxygen in ZnO, which also may include additional oxygen in the grain boundaries such as chemisorbed oxygen.[31−33] It is worth mentioning that the PL results do confirm the presence of both doubly ionized oxygen vacancies and interstitial oxygen in the calcined samples. Therefore, we assume that the O1S band corresponding to O3 is due to the presence of interstitial oxygen in our samples. Thus, our PL data corroborate well with the XPS results confirming the presence of doubly ionized oxygen vacancies in the 300 °C annealed samples and interstitial oxygen in the 600 °C annealed samples. Hence, it can be confirmed that even though the 300 °C annealed sample contains oxygen vacancy defects, extending this analysis to Figure 5b suggests that the concentration of defects appears to be smaller in the 300 °C annealed sample as compared to others. The photoluminescence and Raman spectroscopic studies also confirmed that the 300 °C annealed rods have minimum defects with improved crystal quality supporting the XPS analysis.

**Electron Paramagnetic Resonance Studies.** To further investigate the intrinsic defect centers present in the prepared ZnO rods, EPR studies have been carried out on few selected samples. In Figure 6a−e, the EPR spectra recorded at room temperature for the as-prepared, 300, 400, 500, and 600 °C annealed samples, respectively, are presented. Both the as-prepared and the 300 °C annealed sample exhibited a strong single EPR line at $g$ = 1.954 (inset), whereas in the 400 °C annealed sample the observed signal is very weak, and in the 600 °C annealed sample the EPR signal was completely absent. The origin of this intrinsic EPR signal at $g$ = 1.954 has been controversially discussed in the literature due to singly ionized oxygen vacancies, Zn vacancies, or oxygen or zinc interstitials.[26] To rule out the presence of singly ionized oxygen vacancies in our samples, we carried out magnetic measurements at room temperature (RT) on the rod samples. Both Zn interstitials and oxygen vacancies are known to be the predominant ionic defect types donating electrons and thereby exhibit RT ferromagnetism in ZnO. All of our samples exhibited diamagnetism at room temperature, which was indirect evidence for the absence of either paramagnetic singly ionized oxygen vacancies or zinc interstitials in our samples.[26,34,35]In addition, recent studies confirmed an EPR signal around $g$ = 1.995 as the only signature of singly ionized oxygen vacancies, which again was absent in our samples.[24] Interestingly, many theoretical and experimental studies revealed the presence of isolated hydrogen as hydrogen interstitial $\mathrm{H}i^{+}$ or hydrogen trapped within the oxygen vacancy, $H_O$, in ZnO, both acting as shallow donors giving rise to an EPR signal at 1.95.[36−39] The observed EPR signal at 1.950−1.949 from our samples could thus be assigned to shallow donor centers related to the incorporation of hydrogen in the solution processed ZnO.[36−38] It is interesting to note that the intensity of the EPR signal at $g$ = 1.949 is highest for the 300 °C annealed sample, which decreases substantially at higher annealing temperatures, confirming the loss of hydrogen and thus the shallow door concentrations at higher annealing temperatures. The observed EPR signal was very weak for the 400 °C samples and was completely absent for the 500 and 600 °C annealed samples, thereby confirming the absence of the donor sites in the samples that have been annealed beyond 400 °C.

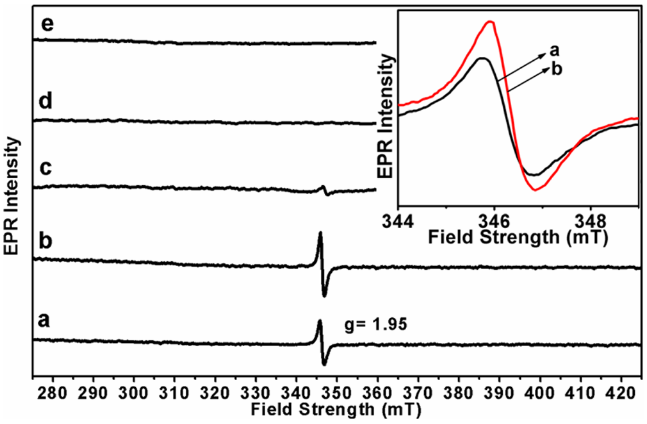

**Figure 6.** EPR spectra measured at room temperature for (a) as-prepared, (b) 300, (c) 400, (d) 500, and (e) 600 °C annealed, respectively. Inset shows the normalized intensity plot of samples (a) and (b).

**Defect Structure of ZnO.** The control of defects is of paramount importance in employing ZnO for various opto-electronic applications.[24] ZnO exhibits both UV and visible emissions spanning a wavelength range of 350−700 nm. The defect related visible emission in most of the cases however is attributed to surface defects; the origin of such emissions is still under controversy despite the large number of reviews and publications.[24−26,33,40] The possible point defect centers in ZnO are (i) zinc vacancies ($V_{zn}$), (ii) zinc interstitials ($Zn_i$), (iii) oxygen interstitials ($O_i$), and (iv) oxygen vacancies ($V_o$). Among these defect centers, zinc interstitial is reported to be diamagnetic.[24,38−40] The oxygen vacancies exist in three different forms such as $V_O^{\circ}$, $V_O^{+}$, and $V_O^{2+}$. There are no unpaired electrons left in the doubly positively charged oxygen vacancy, and hence it is diamagnetic. The oxygen vacancy designated as $V_O^{+}$ is paramagnetic. The neutral $V_O$ defect center captures two electrons and is again diamagnetic in most of the cases. Similarly, oxygen interstitial could be $O_i$, $O_i^{-}$, and $O_i^{2-}$. In this case again, only the $O_i^{-}$ is paramagnetic.[38] The defect related emissions generally occur near the blue-green (450−550 nm) corresponding to singly ionized oxygen vacancies ($V_O^{+}$), yellow (550−610 nm) corresponding to doubly ionized oxygen vacancies ($V_O^{2+}$), and orange-red (610−750 nm) corresponding to interstitial oxygen ($O_i$), respectively.[35] There is a possibility of different kinds of defects coexisting in the same sample giving rise to broad emission in the visible region as in this case.

The band edge emission of ZnO was reported to occur between 373 and 390 nm depending on the structure of the ZnO nanomaterials.[40] In our case, the band edge emission was present at 378 nm for the as-prepared and 383 nm for the 300 °C annealed rods (Figure 3a−g). The minor shift in the band edge emission is assumed to be due to the influence of native defects present on the surface of ZnO rods. In addition to this shift in NBE, we also noticed a significant variation in the NBE band intensity with annealing temperatures (Figure 3). The intensity of the NBE band varied from 1 for the as-prepared sample to 3.78 for 100 °C annealed to 4.91 for 200 °C to 5.81 for 300 °C to 0.63 for 400 °C to 0.57 for 500 °C to 0.41 for the 600 °C annealed samples. An enhancement of NBE with annealing temperature was reported earlier by Huang et al., for the solution processed ZnO rods,[41,42] and they attributed this to an annealing-induced activation and dissociation of shallow hydrogen donor ($H_O^{+}$) trapped within the oxygen vacancies. We also noticed such a substantial increase in the NBE on annealing up to 300 °C. On the other hand, a further increase in annealing temperature has resulted in a reduction in the intensity of the NBE band. As has been reported by Huang et al., at higher temperatures (>425 °C) the hydrogen starts to diffuse away, resulting in a decrease in the NBE emission. Interestingly, we have noticed this change at a lower temperature and confirmed this variation in the NBE to the incorporation and removal of hydrogen during annealing.[41]

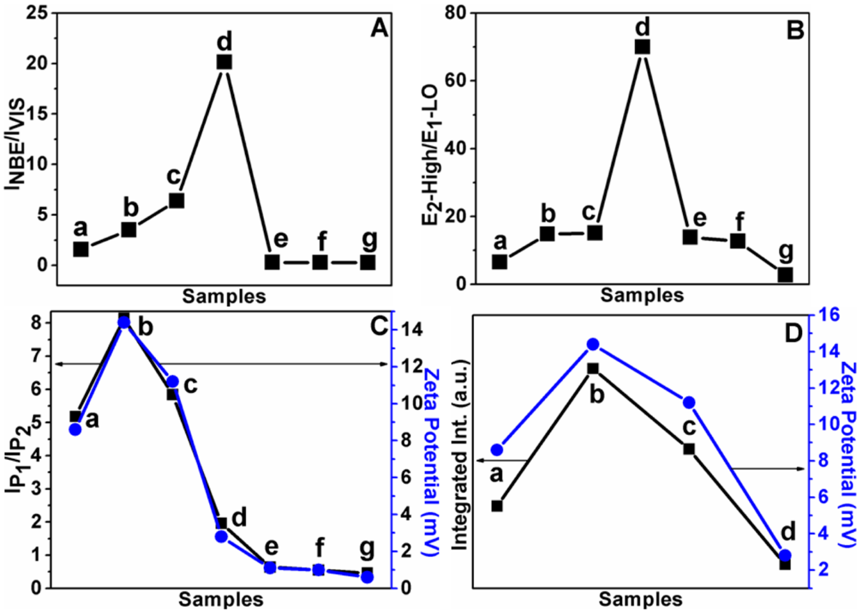

**Figure 7.** (A) The variation of $I_{NBE}/I_{VIS}$ calculated from the emission data shown in Figure 3. (B) $E_2$-high/$E_1$-LO ratio from the Raman data shown in Figure 4. (C) The variation of the relative intensity of the spectral components calculated from the deconvoluted data shown in Supporting Information Figure S4 and the measured zeta potential values for (a) as-prepared, (b) 100, (c) 200, (d) 300, (e) 400, (f) 500, and (g) 600 °C, respectively, annealed samples. (D) The variation of the integrated intensity of the P1 component with the measured zeta potential for (a) as-prepared, (b) 100, (c) 200, and (d) 300 °C annealed samples.

The EPR studies (Figure 6) on the annealed samples corroborate the PL studies, thereby confirming the escape of hydrogen during annealing at temperatures above 300 °C.

With annealing, the visible band maxima slowly shifted from 567 nm for the as-prepared ZnO (2.1 eV) to 569 nm for 100 °C (2.1789 eV) to 570 nm for 200 °C (2.1751 eV) to 590 nm for 300 °C (2.1014 eV) to 612 nm for 400 °C (2.022 eV) to 615 nm for 500 °C (2.0160 eV) and finally to 622 nm for 600 °C (1.993 eV). The broad visible yellow emission of the as-prepared ZnO rods in the 550−610 nm range with a band maximum around 567 ± 2 nm (2.186 eV) is attributed to doubly ionized oxygen vacancies.[32] Moreover, the absence of any emission band in the blue green region confirms the absence of singly ionized oxygen vacancies in the low temperature annealed samples. The broad band in the 490−750 nm region with a band maximum corresponding to orange red emission at 625 nm is attributed to the presence of interstitial oxygen also in the samples.[32,43,44] On annealing at temperatures above 300 °C, the surface oxygen vacancy defects ($Vo^{\cdot\cdot}$) get eliminated, and a subsequent increase in the interstitial oxygen defects ($V_{Oi}''$) occurs. Because of the competition between the above two point defects corresponding to the yellow emission and the red emission, there are overlaps with a shift in the emission peak toward the red as revealed in the case of annealed rods.

The optical properties of the prepared rods were further evaluated by a comparison of the ratio of the intensities of the NBE emission to the visible emission ($I_{NBE}/I_{VIS}$). As is evident from Figure 7A, the $I_{NBE}/I_{VIS}$ ratio of the rods increased to 300 °C and then reduced, on further increase in the annealing temperature. The higher $I_{NBE}/I_{VIS}$ ratio of the 300 °C annealed sample demonstrates the formation of ZnO rods with a lower defect concentration at this particular processing condition. Increase in this ratio with annealing temperature further predicts that the emission center is predominantly located near the surface. Many researchers have reported annealing-dependent variation of PL intensity and confirmed that ZnO nanoparticles annealed at 250 °C exhibit maximum PL intensity and elimination of oxygen vacancies and introduction of oxygen interstitials above 300 °C.[45−47]

To further evaluate the crystal quality of the ZnO, the integrated intensity ratios of E2 (high) to E1 (LO) mode from Raman spectra were calculated and plotted as a function of the annealing temperatures (Figure 7B).[29] The E2 to EI (LO) ratio has been shown to increase with annealing temperature up to 300 °C, and beyond which it decreases further. This change again is a consequence of the decrease of surface defects with annealing temperature with the 300 °C sample exhibiting the minimum concentration of surface defects. To get more insight into the root cause of the visible emission exhibited by the low temperature annealed samples, we have deconvoluted the visible emission bands and fitted the PL band into two individual Gaussian peaks as shown in Supporting Information Figure S4. The two bands are designated as P1 and P2 in Supporting Information Figure S4. The band maxima of P1 for the as-prepared and samples annealed at 100, 200, and 300 °C were located around 550−560 nm (2.254 −2.214 eV), which shifted to 590−600 nm (2.10−2.06 eV) for samples annealed at 400, 500, and 600 °C, respectively. On the contrary, the band P2 located around 625 nm (1.97 eV) was almost absent for the low temperature annealed samples and stronger for the high temperature annealed samples. As discussed earlier, the defect related singly ionized oxygen vacancies ($V_O^+$) generally occur near the blue-green region (450−550 nm), doubly ionized oxygen vacancies ($V_O^{2+}$) occur near the yellow region (550−610 nm), and that corresponding to interstitial oxygen ($O_i$) occurs in the orange-red (610−750 nm) region.[35,47] It has been reported that $V_O^{2+}$ is created by capture of a hole by the $V_O^+$ in a depletion center leading to emission near 550 nm, which is the P1 line in the deconvoluted graph in our case. In this context, it is interesting to quote the work of Ghosh et al., correlating the change in the surface charge/surface potential (zeta potential $\xi$) of the ZnO nanoparticles to the variation in the visible emission intensity.[48,49] The measured zeta potentials of our samples at 20 °C were 8.6, 14.4, 11.2, 2.8, 1.1, 1, and 0.6 mV, respectively, for the as-prepared and samples annealed at 100, 200, 300, 400, 500, and 600 °C, respectively. We have also calculated the ratio of the intensity of the two deconvoluted peaks ($I_{P1}/I_{P2}$) representing the contribution of mainly the doubly ionized oxygen vacancy ($I_{P1}$) and the interstitial oxygen ($I_{P2}$) present in the samples. The calculated ratio ($I_{P1}/I_{P2}$) was 5.18, 8.14, 5.84, 1.96, 0.64, 0.55, and 0.46, for the as-prepared and annealed samples at 100, 200, 300, 400, 500, and 600 °C, respectively. It is interesting to notice the variation in the zeta potential with $I_{P1}/I_{P2}$ ratio shown in Figure 7C. In our case, the samples annealed at 100 °C exhibited the highest zeta potential of 14.4 mV corresponding to an $I_{P1}/I_{P2}$ ratio of 8.14. This shows that the component corresponding to the $IP_1$ arising from doubly ionized oxygen vacancy is maxima in the 100 °C annealed sample. It is also very exciting to note the lower zeta potential (2.8 mV) value exhibited by the 300 °C annealed sample corresponding to an $I_{P1}/I_{P2}$ ratio of 1.96. The samples annealed above 300 °C exhibited very low zeta potential values, confirming almost an absence of the presence of doubly ionized oxygen vacancies on the surface. We have also plotted the zeta potential versus the integrated intensity of the deconvoluted band emission peak P1 as shown in Figure 7D. This result unequivocally confirms the presence of (i) doubly ionized oxygen vacancies in the surface of low temperature annealed samples corresponding to a positive surface charge and zeta potential value and (ii) the presence of lowest concentration of oxygen vacancies in the 300 °C annealed sample and highest in the 100 °C annealed sample.

A comparison of the intensities of the UV emission to the visible emission ($I_{NBE}/I_{VIS}$) of the 300 °C samples annealed in different atmospheres was 30.96 in hydrogen and 57.62 in oxygen as compared to 20.97 in air. These samples also exhibited reduced zeta potential values of 2.5 and 1.9, respectively. These results confirmed a reduction in the defect related emission corresponding to doubly ionized oxygen vacancies during annealing in hydrogen and oxygen atmospheres. As expected, annealing in oxygen was expected to decrease the concentration of oxygen vacancies as $^1/_2O_2 + V_O{}^x = O_O{}^x$. Similarly, annealing in hydrogen could result in trapped hydrogen within the oxygen vacancies and form shallow donors of the type $H_O$ and thus reduce the oxygen vacancy defect related emission further. The above atmosphere controlled annealing experiments unequivocally indicated the presence of oxygen vacancies in the 300 °C annealed samples. All of the experimental evidence taken together suggests the presence of doubly ionized oxygen vacancies in the low temperature annealed samples and oxygen interstitial in the high temperature annealed samples.

**Infrared, UV, and Diffuse Reflectance Studies.** The IR spectra show an absorption band at ~520 $cm^{-1}$ for all three samples (Supporting Information Figure S5A), characteristic of Zn−O band stretching frequency.[50] In addition, a broad stretching band at ~3450 $cm^{-1}$ and a corresponding bending mode band around 1600 $cm^{-1}$ have been found in the spectrum of the as-prepared rods corresponding to the O−H stretching vibration of molecularly adsorbed $H_2O$.[51] The intensity of the 3450 $cm^{-1}$ peak significantly reduces with annealing and essentially disappears for the 600 °C sample under ambient condition. As discussed in the Raman spectrum, the $A_1$, $E_1$, and $E_2$ optic modes are Raman active, but the $A_1$ and $E_1$ modes are IR active too.[51] We have seen a clear broadening in the Zn−O stretching mode with an indication of a splitting with increase in annealing temperature. The as-prepared sample exhibited a Zn−O bond stretching around 539 $cm^{-1}$, which is seen to shift to 518 $cm^{-1}$ for the 300 °C and to 522 $cm^{-1}$ for the 600 °C annealed sample. The presence of oxygen defects could weaken the Zn−O bond strength, resulting in a shifting of the IR absorption band toward lower wavenumber. The observed IR data further confirm the lower concentration of oxygen defects in the 300 °C annealed ZnO rods. The additional significant peaks at ~1365 and 1602 $cm^{-1}$ (Supporting Information Figure S5B) correspond to the symmetric and asymmetric C−O stretching vibration from the carboxylate groups, confirming the successful adsorption of the dye molecule. The weak band at 2109 $cm^{-1}$ corresponds to the NCS stretching band of the thiocyanate ligand in N719 dye molecule.[52] These indicate successful adsorption of dye molecules on the ZnO surface.[14,53]

To study the dye adsorbing capability of the studied ZnO samples, a known amount of the ZnO has been soaked in 0.5 mM N719 dye solution in ethanol for 4 h. The absorption spectra of an ethanolic solution of N719 dye molecule and the desorbed dye molecules collected after dye absorption on the ZnO samples are presented in Supporting Information Figure S6. The dye molecule exhibits three distinct peaks at 310, 380, and 524 nm, respectively. The 380 and 524 nm peaks are due to the MLCT bands and the highest energy peak at 310 nm, which is actually a doublet due to the $\Pi \rightarrow \Pi^*$ intraligand transition. It is worth noting a blue shift of the 524 nm peak after interaction with ZnO powders probably indicating the possible formation of ZnO/dye aggregates. It is clear that the intensity of the residual dye solution is highest for the ZnO powder annealed at 600 °C and is lowest for the as-prepared sample. The percentage of the dye adsorbed on the ZnO rod surface could be expressed by the formula $(C_o - C)/C_o$, where $C_o$ is the initial concentration of the N719 dye and $C$ is the percentage of residual dye in the solution.[54] It can be concluded that the dye adsorption ability, $(C_o - C)/C_o$, is highest for the as-prepared ZnO and gradually decreases for the 300 and 600 °C annealed samples. The surface areas of the samples were 2.3, 1.9, and 1 $m^2/g$, respectively, for the as-prepared, 300, and 600 °C annealed samples.

The diffuse reflectance (DR) spectra of the free ZnO powders and those impregnated with 0.5 mM N719 dye in ethanol for 4 h at room temperature are presented in Supporting Information Figure S7. The reflectance of the as-prepared and the 300 °C annealed rods is high as compared to that of the 600 °C annealed rods, indicating high light scattering ability of the former samples. An abrupt decrease in reflectance at a wavelength around ~380 nm corresponds to the interband absorption of ZnO rods. The higher dye loading capability of the as-prepared rods could be due to the hydrophilic surface property of the as-prepared rods. Despite a larger rod length (Figure 1b and c), the DR spectrum indicates a lower dye adsorption for the 300 °C annealed samples, probably due to the lower OH content on the samples. This was further revealed from the IR studies discussed above. The DR spectrum of 300 °C annealed rods, on the other hand, indicates a higher light scattering ability as compared to the as-prepared rods after dye loading. The surface of a dye adsorbed film is shown as an inset in Supporting Information Figure S7, indicating no morphological change after dye adsorption.

To find out the contribution of charge carriers present in our samples, we have monitored the $I-V$ characteristics of the fabricated films. Current perpendicular-to-plane (CPP) conductivity measurements were performed on all ZnO films before dye loading using aluminum top electrode as shown in Supporting Information Figure S8. Here, the voltage was swept from 0 to 6 V with a step of 0.5 V. From the measurements, it was clear that 300 °C annealed films are more conducting as compared to the as-prepared and 600 °C annealed samples. These data corroborate well with our findings from EPR measurements confirming the presence of donor defects in the prepared ZnO samples, with a higher signal intensity for the 300 °C annealed sample. Mostly, the donor defects have been reported to be responsible for the n-type conductivity in ZnO.[36,37]

**DSSC Measurements.** The isoelectric point (IEP) of ZnO is 9, and hence the dissolution of Zn ions and formation of $Zn^{2+}$/dye aggregates occurs with acidic dye molecules. Therefore, we examined the performance of the ZnO rods with N719 dye molecules having lower number of carboxyl groups than N3 dye.[14] Figure 8 shows the $J$−$V$ characteristics of the DSSCs fabricated with the as-prepared and annealed ZnO rods as photoanodes. The fill factor (FF) of the DSSC was calculated using eq 3:[55]

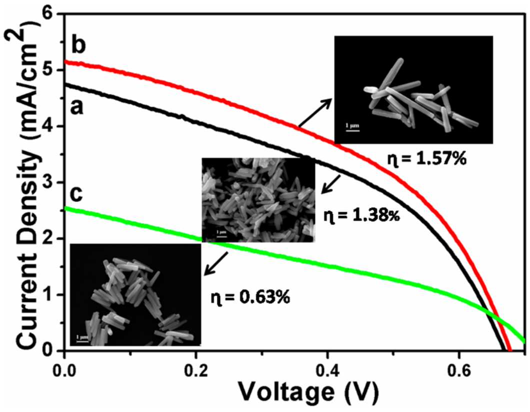

**Figure 8.** Current density ($J$)−voltage ($V$) curve of DSSCs fabricated with (a) as-prepared, (b) 300 °C, and (c) 600 °C annealed ZnO rods.

$$\text{fill factor} = \frac{I_{\max}V_{\max}}{I_{\mathrm{sc}}V_{\mathrm{oc}}} \tag{3}$$

where $I_{\max}$ and $V_{\max}$ are the current and voltage obtained, respectively, at the maximum power point on the photovoltaic power output curve. The FF can be increased by reducing the recombination between the photo excited carriers at the ZnO nanostructures and the tri-iodide ions in the electrolyte. The photovoltaic efficiency ($\eta$) was calculated by eq 4:

$$\eta = \frac{I_{\mathrm{SC}}V_{\mathrm{OC}}\mathrm{FF}}{P_{\mathrm{in}}} \tag{4}$$

$P_{\mathrm{in}}$ is the solar radiation intensity/intensity of the incident light.

**Table 1. Photovoltaic Performance of the ZnO Rods**

| sample | $V_{\mathrm{oc}}$ (V) | $J_{\mathrm{sc}}$ (mA/cm$^2$) | FF (%) | efficiency ±0.2 (%) |
|---|---|---|---|---|
| as-prepared ZnO rods | 0.66 | 4.73 | 43.58 | 1.38 |
| annealed at 300 °C | 0.67 | 5.11 | 45.29 | 1.57 |
| annealed at 600 °C | 0.71 | 2.5 | 35.2 | 0.63 |

The thickness of the ZnO photoanode was optimized first as the $V_{\mathrm{OC}}$ and $I_{\mathrm{SC}}$ of the DSSC depend on the thickness of the films. The open circuit voltage $V_{\mathrm{oc}}$ of a DSSC is the difference between the Fermi energy of the semiconductor ZnO and the redox potential of the electrolyte. The $V_{\mathrm{OC}}$ can increase with increase in the thickness, while the $I_{\mathrm{SC}}$ will decrease as the layer thickness increases. As is evident from the data summarized in Table 1, a strong influence of annealing on the cell performance was noticed. The rods annealed at 300 °C exhibited a higher current density, fill factor, and efficiency as compared to the as-prepared and 600 °C annealed samples. The cell efficiency varied in the order 300 °C rods > as-prepared rods > 600 °C rods as 1.57% > 1.38% > 0.63%, respectively. The fill factor was highest for 300 °C annealed and minimum for the 600 °C annealed rods. It can be seen that there is no direct relation between the amount of dye adsorbed and the efficiency values because the DR data show maximum dye loading on the as-prepared samples probably due to the higher surface hydroxyls. The 600 °C annealed sample exhibited the lowest dye loading capability and consequently the lowest efficiency. In addition, the sample annealed at 600 °C, that is, the one exhibiting orange red emission, exhibited lower short circuit current density $J_{\mathrm{sc}}$, higher open circuit voltage $V_{\mathrm{oc}}$, and lower fill factor as compared to those exhibiting green yellow emission or weak emission in the visible. In accordance with the PL results, the ZnO rods annealed at 600 °C contain mainly the chemisorbed or interstitial oxygen. This sample exhibited a higher open circuit voltage ($V_{\mathrm{oc}}$) of 0.71 V and a lower fill factor (FF) of 35.2. The lower free carrier density in the 300 °C annealed sample could induce a positive shift of the Fermi level of ZnO rods that could further reduce the gap between the $I^-/I^{3-}$ redox couple and Fermi level, thereby minimizing the $V_{\mathrm{oc}}$ followed by an improvement in fill factor, which is less recombination and thereby enhances the efficiency indirectly.[19,20,56,57] The as-prepared and 300 °C annealed ZnO rods having less oxygen vacancy density exhibited relatively less $V_{\mathrm{oc}}$ of 0.66 and 0.67 V, respectively (Figure 8a) and a higher fill factor of 43.58% and 45.29%, respectively (Figure 8c). The photoluminescence and Raman spectroscopic studies confirmed that the 300 °C annealed rods have minimum defects with improved crystal quality. The favorable surface condition for dye adsorption (hydrophilic due to OH), improved crystallinity, better light scattering ability, and less oxygen vacancy density collectively account for a higher electron injection to the conduction band of ZnO rods annealed at 300 °C resulting in a maximum short circuit current density ($J_{\mathrm{sc}}$) of 5.11 mA/cm$^2$ and consequently a higher overall conversion efficiency of 1.57% (Figure 8b). We also accomplished a reasonable overall conversion efficiency of 1.38% with a short circuit current of 4.73 mA/cm$^2$ from the fabricated DSSCs with the as-prepared ZnO rods.

Although the synthesis and DSSC performance of various solution-derived ZnO rods have been reported in a series of reviews and articles, the efficiencies of most of them were below 1% with a few exhibiting above 1% efficiency.[58−63] In this respect, our data are far superior in that we were able to prepare ZnO rods by a very simple solution technique without the use of any surfactant or structure-directing agent exhibiting much enhanced DSSC efficiency as compared to many of the reported values on solution processed ZnO rods.[18−20,58−63]

**Impedance Measurements.** The impedance measurements were performed on the samples to learn more about the transport properties at different interfaces in the solar cell assembly. The frequency range chosen for the measurement was from $10^{-2}$ to $10^6$ Hz with an AC amplitude of 10 mV. As is

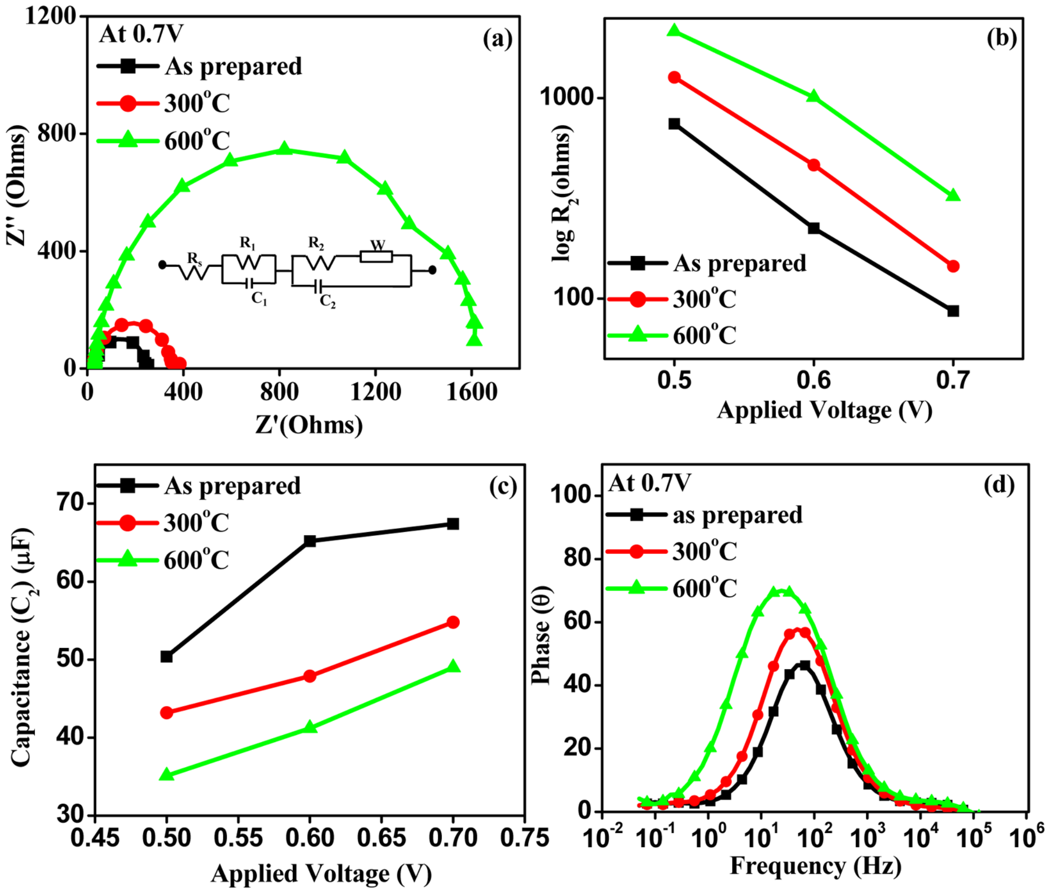

**Figure 9.** Impedance analysis of all three cases: (a) Nyquist plot measured at 0.7 V and equivalent circuit used for fitting, (b) log $R_2$ versus applied voltage, (c) capacitance ($C_2$) versus applied voltage, and (d) Bode plot measured at 0.7 V.

well-known, the typical Nyquist plot for DSSC consists of three semicircles representing the three different interfaces. The first semicircle shows the Pt/electrolyte interface, the second semicircle depicts the ZnO/dye/electrolyte interface, and the third describes the diffusion of $I^-/I_3^-$ and Warburg impedance.[64] As the Pt and electrolyte used are the same for all cases, the interface of our interest for the sake of comparison is the ZnO/dye/electrolyte interface, where ZnO used was as-prepared or annealed at different temperatures as described earlier. The impedance data were recorded at three different bias voltages. From the recorded Nyquist plots, the resistance and capacitance values were extracted for an equivalent circuit,[13] shown in Figure 9a. Figure 9b shows the plot of log of resistance ($R_2$) versus the applied voltage, $R_2$ being the charge transfer resistance including the effects of recombination of electrons with $I_3^-$ at the ZnO/electrolyte interface. $R_2$ is lowest for the as-prepared case, and is seen to increase with annealing temperature. The behavior of the capacitance $C_2$ (in parallel to $R_2$ in the equivalent circuit) is shown in Figure 9c and is seen to be opposite to that of $R_2$. This capacitance describes the storage of charges upon injection of electrons from the dye molecule to ZnO. The Bode plot (Figure 9d) was also recorded to calculate the electron lifetimes. The peak frequency of central arc $k_{\mathrm{eff}}$ describes the rate of recombination of electrons in the film. It was 57.7 $s^{-1}$ for the as-prepared sample, 47.7 $s^{-1}$ for the 300 °C annealed sample, and 33.8 $s^{-1}$ for the 600 °C annealed sample. The lifetimes were thus 2.7, 3.3, and 4.7 ms, respectively, for the as-prepared, 300, and 600 °C annealed samples, respectively. Clearly, the lifetime of electrons is lowest in the as-prepared sample and increases with annealing temperature.

The data presented in Figure 9b establish that the transport parameters are basically following a monotonic trend as a function of annealing temperature. Thus, the possible origin for nonmonotonic behavior of conversion efficiency (it being highest for 300 °C annealed sample) has to be sought elsewhere. We looked at the dye adsorption capability in the case of the three samples. As discussed earlier, the dye adsorption was also found to follow a monotonic trend. It thus seems reasonable to assume, on the basis of the PL data presented in Figure 3, that the presence of minimum concentration of surface defects in the case of the 300 °C annealed sample with a sharp band edge exciton contribution without any significant bound exciton contribution(s) should be responsible for the higher efficiency. The as-prepared and 600 °C annealed samples are seen to exhibit fairly strong bound exciton PL contributions, although they are characteristically different. Although the electron lifetime was higher in the 600 °C annealed case, if this is much shorter than the transport lifetime, then the efficiency could be lower in this case as compared to the 300 °C annealed case. The transport lifetimes estimated for the 300 and 600 °C annealed samples at 0.7 V were 14.4 and 9 ms, respectively. Thus, for both cases, the recombination effects in the interconnected ZnO network seem to dominate the transport process. As emphasized by Wong et al., the conversion efficiency is a truly complex function of several of these parameters, and further work would be needed to offer definitive answers in this respect.[18]

## CONCLUSIONS

The effect of post annealing temperatures on the DSSC performance of solution-grown ZnO rods has been studied in detail. Detailed characterization of the studied ZnO based on Raman spectroscopy, infrared spectroscopy, photoemission spectroscopy, and photoluminescence studies confirmed that annealing at 300 °C results in ZnO rods with minimum surface defects and a sharp band edge exciton contribution. It was also observed that the 300 °C annealed sample contains high shallow donor concentrations as compared to as-prepared and high temperature annealed samples. We also noticed a correlation between the surface charges and the zeta potential exhibited by the rods and the oxygen vacancy related visible defect emission. On the basis of our results, we were able to conclude that solution processed ZnO rods exhibiting the lowest visible emission corresponding to minimum structural defects are better suited for fabricating DSSC with improved efficiency (1.57%), current density (5.11 mA/cm$^2$), and fill factor 45.29%. We have also carried out electrochemical impedance measurements to understand the transport properties at different interfaces in the solar cell assembly. Finally, it could be confirmed that the improved efficiency of the 300 °C annealed rods is due to the reduction in the recombination centers present on ZnO surfaces. It is confirmed that, irrespective of the nature of the samples, a higher amount of dye adsorption is not the key step, but controlling the native defects is the most important key step in achieving higher efficiency from solution synthesized ZnO-based photoanode.

## ASSOCIATED CONTENT

### Ⓢ Supporting Information

Additional lattice parameters, X-ray diffraction data, absorption data, emission data of annealed samples, infrared spectral data, dye absorption graph, diffuse reflectance, and *I*−*V* data. This material is available free of charge via the Internet at http://pubs.acs.org.

## AUTHOR INFORMATION

### Corresponding Author

*Tel.: +91-33-2483-8082. Fax: +91-33-2473-0957. E-mail: psujathadevi@cgcri.res.in, psujathadevi@gmail.com.

### Notes

The authors declare no competing financial interest.

## ACKNOWLEDGMENTS

P.S.D. and S.B.O. acknowledge MNRE for financial support under CSIR-TAPSUN program. P.P.D. acknowledges the financial support of MNRE to carry out the Ph.D. program. S.M. thankfully acknowledges the University Grants Commission (UGC) Government of India for the award of Junior Research Fellowships through the National Eligibility Test. P.S.D. thanks Prof. Prasanta Ghosh, Department of Chemistry, R. K. Mission Residential College, Narendrapur Kolkata for helping us with EPR measurements. We also thank all of the anonymous reviewers for their valuable suggestions that enabled us to improve this manuscript considerably.

## REFERENCES

(1) Oregan, B.; Gratzel, M. *Nature* **1991**, *353*, 737−740.
(2) Gratzel, M. *J. Photochem. Photobiol. C* **2003**, *4*, 145−153.
(3) Gratzel, M. *Inorg. Chem.* **2005**, *44*, 6841−6851.
(4) Burschka, J.; Pellet, N.; Moon, S. J.; Baker, R. H.; Gao, P.; Nazeeruddin, M. K.; Gratzel, M. *Nature* **2013**, *499*, 316−319.
(5) Hagfeldt, A.; Boschloo, G.; Sun, L.; Kloo, L.; Pattersson, H. *Chem. Rev.* **2010**, *110*, 6595−6663.
(6) Zhang, Q.; Dandeneau, C. S.; Zhou, X.; Cao, G. *Adv. Mater.* **2009**, *21*, 4087−4108.
(7) Anta, J. A.; Guillen, E.; Zaera, R. T. *J. Phys. Chem. C* **2012**, *116*, 11413−11425.
(8) Xu, F.; Sun, L. *Energy Environ. Sci.* **2011**, *4*, 818−841.
(9) Baskoutas, S.; Bester, G. *J. Phys. Chem. C* **2012**, *114*, 9301−9307.
(10) He, C. H.; Lei, B. X.; Wang, Y. F.; Su, C. Y.; Fang, Y. P.; Kuang, D. B. *Chem.—Eur. J.* **2010**, *16*, 8757−8761.
(11) Shi, Y.; Zhu, C.; Wang, L.; Zhao, C.; Li, W.; Fung, K. K.; Ma, T.; Hagfeldt, A.; Wang, N. *Chem. Mater.* **2013**, *25*, 1000−1012.
(12) Yang, W.; Wan, F.; Chen, S.; Jiang, C. *Nanoscale Res. Lett.* **2009**, *4*, 1486−1492.
(13) Lai, H. Y.; Lin, Y. C.; Chen, W. H.; Chen, G. J.; Kung, W. C.; Vittal, R.; Ho, K. C. *J. Mater. Chem.* **2010**, *20*, 9379−9385.
(14) Thavasi, V.; Renugopalakrishnan, V.; Jose, R.; Ramakrishna, S. *Mater. Sci. Eng. R* **2009**, *63*, 81−99.
(15) Law, M.; Greene, E. L.; Johnson, C. J.; Saykally, R.; Yang, D. P. *Nat. Mater.* **2005**, *4*, 455−459.
(16) Shan, P.; Tenegfeng, X.; Yu, Z.; Xiao, W.; Min, Y.; Dejun, W.; Zuliang, D. *J. Phys. Chem. C* **2007**, *111*, 18417−18422.
(17) Hsu, Y. F.; Xi, Y. Y.; Djurisic, B. A.; Chan, K. W. *Appl. Phys. Lett.* **2008**, *92*, 113505−113507.
(18) Wong, K. K.; Ng, A.; Chen, Y. X.; Ng, H. Y.; Leung, H. Y.; Ho, H. K.; Djurisic, B. A.; Ng, C. M. A.; Chan, K. W.; Yu, L.; Philips, D. L. *ACS Appl. Mater. Interfaces* **2012**, *4*, 1254−1261.
(19) Lou, Y. Y.; Yuan, S.; Zhao, Y.; Wang, Z. Y.; Shi, L. Y. *Adv. Manuf.* **2013**, *1*, 340−345.
(20) Makhal, A.; Sarkar, S.; Bora, T.; Baruah, S.; Dutta, J.; Raychaudhuri, A. K.; Pal, S. K. *J. Phys. Chem. C* **2010**, *114*, 10390−10395.
(21) Dhas, V.; Muduli, S.; Lee, W.; Han, S. H.; Ogale, S. *Appl. Phys. Lett.* **2008**, *93*, 243108−243110.
(22) Jana, A.; Sujatha Devi, P.; Mitra, A.; Bandyopadhyay, N. R. *Mater. Chem. Phys.* **2013**, *139*, 431−436.
(23) Li, W. J.; Shi, E. W.; Zhong, W. Z.; Yin, Z. W. *J. Cryst. Growth* **1999**, *203*, 186−196.
(24) Mende, S. L.; Driscoll, L. M. J. *Mater. Today* **2007**, *10*, 40−48.
(25) Ischenko, V.; Polarz, S.; Grote, D.; Stavarache, V.; Fink, K.; Driess, M. *Adv. Funct. Mater.* **2005**, *15*, 1945−1954.
(26) Janotti, A.; Van de Walle, C. G. *Rep. Prog. Phys.* **2009**, *72*, 126501−126530.
(27) Cusco, R.; Llado, A. E.; Ibanez, J.; Artus, L. *Phys. Rev. B* **2007**, *75*, 165202−165212.
(28) Calleja, M. J.; Cardona, M. *Phys. Rev. B* **1977**, *16*, 3753−3761.
(29) Kanamani, S. S.; Ramachandran, K.; Umapathy, S. *Int. J. Photoenergy* **2012**, *267824*, 1−8.
(30) Yang, J. X.; Miao, Y. X.; Xu, L. X.; Xu, M. C.; Xu, J.; Liu, T. H. *J. Opt. Mater.* **2005**, *27*, 1602−1605.
(31) Kukreja, L. M.; Misra, P.; Fallert, J.; Phase, D. M.; Kalt, H. *J. Appl. Phys.* **2012**, *112*, 013525−013532.
(32) Fan, J.; Hao, Y.; Munuera, C.; Hernández, M. G.; Güell, F.; Johansson, E. M. J.; Boschloo, G.; Hagfeldt, A.; Cabot, A. *J. Phys. Chem. C* **2013**, *117*, 16349−16356.
(33) Ramgir, N. S.; Late, D. J.; Bhise, A. B.; More, M. A.; Mulla, I. S.; Joag, D. S.; Vijayamohanan, K. *J. Phys. Chem. B* **2006**, *110*, 18236−18242.
(34) Panigrahy, B.; Aslam, M.; Misra, D. S.; Ghosh, M.; Bahadur, D. *Adv. Funct. Mater.* **2010**, *20*, 1161−1165.
(35) Podila, R.; Queen, W.; Nath, A.; Arantes, T. J.; Schoenhalz, L. A.; Fazzio, A.; Dalpian, M. G.; He, J.; Hu, S. J.; Skov, J. M.; Rao, A. M. *Nano Lett.* **2010**, *10*, 1383−1386.
(36) Du, M. H.; Biswas, K. *Phys. Rev. Lett.* **2011**, *106*, 115502−115505.

(37) Hofman, D. M.; Hofstaetter, A.; Leiter, F.; Zhou, H.; Henecker, F.; Meyer, K.; Orlinskii, S. B.; Schmidt, J.; Baranov, P. G. *Phys. Rev. Lett.* **2002**, *88*, 045504−045508.
(38) Lavrov, E. V.; Herklotz, F.; Weber, J. *Phys. Rev. B* **2009**, *79*, 165210−165222.
(39) Jinpeng, Lv.; Chundong, Li.; BelBruno, J. J. *CrystEngComm* **2013**, *15*, 5620−5625.
(40) Kaftelen, H.; Ocakoglu, K.; Thomann, R.; Tu, S.; Weber, S.; Eedem, E. *Phys. Rev. B* **2012**, *86*, 0141131-1−8.
(41) Huang, X. H.; Tay, C. B.; Zhang, C.; Zheng, L. X.; Venkatesan, T.; Chua, S. J. *CrystEngComm* **2011**, *13*, 7032−7036.
(42) Huang, X. H.; Zhan, Z. Y.; Pramoda, K. P.; Zhang, C.; Zheng, L. X.; Chua, S. J. *CrystEngComm* **2012**, *14*, 5163−5165.
(43) Djurisic, A. B.; Choy, W. C. H.; Roy, V. A. L.; Leung, Y. H.; Kwong, C. Y.; Cheah, K. W.; Rao, T. K. G.; Chan, W. K.; Lui, H. F.; Surya, C. *Adv. Funct. Mater.* **2004**, *14*, 856−864.
(44) Djurisic, B. A.; Leung, Y. H. *Small* **2006**, *2*, 944−961.
(45) Bora, T.; Lakshman, K. K.; Sarkar, S.; Makhal, A.; Sardar, S.; Pal, K. S.; Dutta, J. *Beilstein J. Nanotechnol.* **2013**, *4*, 714−725.
(46) Wei, S.; Lian, J.; Wu, H. *Mater. Charact.* **2010**, *61*, 1239−1244.
(47) Tam, H. K.; Cheung, K. C.; Leung, H. Y.; Djurisic, B. A.; Ling, C. C.; Beling, D. C.; Fung, S.; Kwok, M. W.; Chan, K. W.; Philips, L. D.; Ding, L.; Ge, K. W. *J. Phys. Chem. B* **2006**, *110*, 20865−20871.
(48) Ghosh, M.; Raychaudhuri, A. K. *Nanotechnology* **2008**, *19*, 445704−445710.
(49) Ghosh, M.; Raychaudhuri, A. K. *Appl. Phys. Lett.* **2008**, *93*, 123113−123115.
(50) Alvi, N. H.; Hasan, K. U.; Nur, O.; Willander, M. *Nanoscale Res. Lett.* **2011**, *6*, 130−136.
(51) Zheng, Y.; Chen, C.; Zhan, Y.; Lin, X.; Zheng, Q.; Wei, K.; Zhu, J.; Zhu, Y. *Inorg. Chem.* **2007**, *46*, 6675−6682.
(52) Noei, H.; Qiu, H.; Wang, Y.; LÖffler, E.; WÖll, C.; Muhler, M. *Phys. Chem. Chem. Phys.* **2008**, *10*, 7092−7097.
(53) Park, Y.; J, Y. M.; Sarker, S.; Lee, Y.; Lee, K.; Oh, J. J.; Joo, S. W. *Sol. Energy Mater. Sol. Cells* **2010**, *94*, 857−864.
(54) Dell'Orto, E.; Raimondo, L.; Sassella, A.; Abbotto, A. *J. Mater. Chem.* **2012**, *22*, 11364−11369.
(55) Jana, A.; Das, P. P.; Agarkar, S.; Devi, P. S. *Sol. Energy* **2014**, *102*, 143−151.
(56) Wu, K. M.; Ling, T.; Xie, Y.; Huang, G. X.; Du, W. X. *Semicond. Sci. Technol.* **2011**, *26*, 105001−105007.
(57) Etgar, L.; Bendall, S. J.; Laporte, V.; Welland, E. M.; Gratzel, M. *J. Mater. Chem.* **2012**, *22*, 24463−24468.
(58) Seow, Z. L. S.; Wong, A. S. W.; Thavasi, V.; Jose, R.; Ramakrishna, S.; Ho, G. W. *Nanotechnology* **2009**, *20*, 045604−045609.
(59) Kao, M.-C.; Chen, H.-Z.; Young, S.-L.; Lin, C.-C.; Kung, C.-Y. *Nanoscale Res. Lett.* **2012**, *7*, 260−265.
(60) Kislyuk, V. V.; Dimitriev, O. P. *J. Nanosci. Nanotechnol.* **2008**, *8*, 131−148.
(61) Zhang, R.; Kumar, S.; Zou, S.; Kerr, L. L. *Cryst. Growth Des.* **2008**, *8*, 381−383.
(62) Xie, Y.; Joshi, P.; Darling, S. B.; Chen, Q.; Zhang, T.; Galipeau, D.; Qiao, Q. *J. Phys. Chem. C* **2010**, *114*, 17880−17888.
(63) Hajry, A. A.; Umarb, A.; Hahnc, Y. B.; Kimd, D. H. *Superlattices Microstruct.* **2009**, *45*, 529−534.
(64) Halme, J.; Vahermaa, P.; Miettunen, K.; Lund, P. *Adv. Mater.* **2010**, *22*, E210−E234.